FRONTIERS OF PHYSICS

RESEARCH ARTICLE
Volume 18 / Issue 1 / 13305 / 2023

Two dimensional $GeO_2/MoSi_2N_4$ van der Waals heterostructures with robust type-II band alignment

Xueping Li[1,2,3], Peize Yuan[1], Lin Li[2], Ting Liu[2], Chenhai Shen[2], Yurong Jiang[2],
Xiaohui Song[2], Congxin Xia[2,†]

1 College of Electronic and Electrical Engineering, Henan Normal University, Xinxiang 453007, China
2 Department of Physics, Henan Normal University, Xinxiang 453007, China
3 Henan Key Laboratory of Optoelectronic Sensing Integrated Application, Henan Normal University, Xinxiang 453007, China
Corresponding author. E-mail: †xiacongxin@htu.edu.cn

Received September 21, 2022; accepted October 12, 2022

ABSTRACT

Constructing two-dimensional (2D) van der Waals heterostructures (vdWHs) can expand the electronic and optoelectronic applications of 2D semiconductors. However, the work on the 2D vdWHs with robust band alignment is still scarce. Here, we employ a global structure search approach to construct the vdWHs with monolayer $MoSi_2N_4$ and wide-bandgap GeO_2. The studies show that the $GeO_2/MoSi_2N_4$ vdWHs have the characteristics of direct structures with the band gap of 0.946 eV and type-II band alignment with GeO_2 and $MoSi_2N_4$ layers as the conduction band minimum (CBM) and valence band maximum (VBM), respectively. Also, the direct-to-indirect band gap transition can be achieved by applying biaxial strain. In particular, the 2D $GeO_2/MoSi_2N_4$ vdWHs show a robust type-II band alignment under the effects of biaxial strain, interlayer distance and external electric field. The results provide a route to realize the robust type-II band alignment vdWHs, which is helpful for the implementation of optoelectronic nanodevices with stable characteristics.

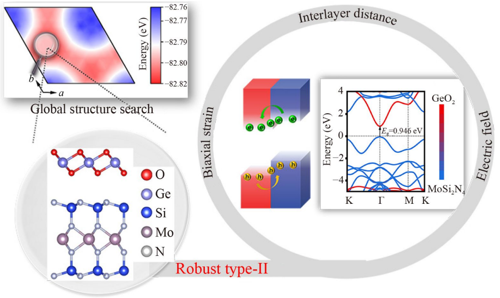

Keywords van der Waals heterostructures, wide gap material, global structure search, robust type-II band alignment

1 Introduction

Two-dimensional (2D) semiconductor and related van der Waals heterostructures (vdWHs) have attracted tremendous attention because they possess excellent characteristics [1–5]. Also, the 2D vdWHs can form different band alignments, such as type-I, II and III, which is useful to diverse device applications [6–9]. Among them, type-II band alignment plays a critical role in facilitating the electron and hole separation, resulting in long photogenerated carrier lifetimes and tunable interlayer coupling [10–13]. However, the type-II band alignments of most 2D vdWHs are sensitive to external conditions [14–16], which brings a challenge for nanodevices to achieve stable properties. Therefore, it is valuable to find 2D vdWHs with robust type-II band alignment.

More recently, $MoSi_2N_4$ monolayer, an ultrathin transition metal nitride, is in the spotlight for its successful synthesis via passivating MoN_2 monolayer with silicon [17]. The $MoSi_2N_4$ monolayer is a seven-layer nanosheet consisting of one MoN_2 inner layer and two Si-N outer layers [18]. Furthermore, $MoSi_2N_4$ is reported to show great potential application due to its superior performance

Higher Education Press

https://doi.org/10.1007/s11467-022-1216-8

[19–31], including the impressive ambient stability [27], large theoretical electron/hole mobility (~270/ 1200 $cm^2 \cdot V^{-1} \cdot s^{-1}$) [17], excellent thermoelectric property [28, 29], and remarkable optical absorption in the visible light range [30, 31]. Stimulated by the excellent performance, the 2D vdWHs based on $MoSi_2N_4$ have become an emerging field [32–41]. For instance, $C_3N_4/MoSi_2N_4$ vdWHs have achieved a tunable type-II band alignment through interlayer coupling and external electric field [38]. The $MoSi_2N_4/NbS_2$ vdWHs have robust ultra-low *p*-type Schottky barrier heights (SBH), while the SBH of $MoSi_2N_4$/graphene can be modulated via the interlayer distance and electric fields [32]. Compared to isolated transition metal dichalogens (TMDs), the $MoSi_2N_4$/ TMDs vdWHs possess higher mobility, improved optical absorption, and tunable band structures [37, 40, 41]. Additionally, Jin *et al.* [42] have found that the vdWHs based on $MoSi_2N_4$ and wide-band gap semiconductors, such as ZnO and GaN, have retained the type-II band alignment when the electric field is smaller, but there is a transition from type-II to type-I band alignment with the application of out-of-plane strain. Among the wide-band gap semiconductors, monolayer GeO_2 features an excitonic gap in the deep ultraviolet (UV) region with an energy of 6.24 eV [43]. It is found that the GeO_2 has a relatively high work function, which is higher than that of reported results for the thin films of transition metal oxides [44] and traditional monolayers of TMDs [45], suggesting that GeO_2 is advisable to be integrated into optical and electronic devices as charge extraction and injection layers that provide improvements in the device ability. Also, the 2D GeO_2 material is fabricated by strictly controlling the degree of oxidation at the metal-gas interface [46].

Considering better lattice mismatch and interesting performance between the GeO_2 and $MoSi_2N_4$ monolayers, and there are few works on GeO_2-based vdWHs, so we select GeO_2 as representative one of wide-band gap semiconductors to construct the heterojunction with $MoSi_2N_4$ and study the corresponding performance. In this work, the most stable structures are obtained by the global structure search method of passing through 12 × 12 displacement grids. Additionally, the robust type-II band arrangement of $GeO_2/MoSi_2N_4$ vdWHs is insensitive to the regulation of biaxial strain, interlayer distance and external electric field, which opens up more possibilities for developing the stable optoelectronic devices.

2 Computational details

All the calculations are gotten via the Vienna *ab initio* simulation package (VASP) based on DFT [47]. With the framework of generalized gradient approximation (GGA), the Perdew–Burke–Ernzerhof (PBE) [48] functional is employed to deal with the exchange-correlation energy, and the Heyd–Scuseria–Ernzerhof (HSE06) method is utilized to gain more precise band gap value [49]. In addition, the projector augmented wave (PAW) pseudopotentials are adopted to simulate the electron-ion potential [50]. The vdW interlayer interaction in the $GeO_2/MoSi_2N_4$ heterostructure is corrected by DFT-D3 correction method. Besides, the out-of-plane vacuum region, about 20 Å, is used, and the plane-wave cutoff is employed as 500 eV. A 11×11×1 k-point mesh is adopted for the sampling in reciprocal space. The structures are relaxed until the Hellmann–Feynman forces and the total energy converge to 0.01 eV/Å and 10^{-5} eV, respectively. Moreover, we would like to point out that the dipole correction is utilized in our calculations.

3 Results and discussion

3.1 Crystal structure and stability of isolated layer and heterojunctions

The geometric structures, band structures and phonon dispersion curves of GeO_2 and $MoSi_2N_4$ monolayers are listed in Fig. 1. Both GeO_2 and $MoSi_2N_4$ monolayers have hexagonal structures, as shown in Figs. 1(a) and (d), and Table 1 demonstrates that the optimized lattice parameters are $a = b = 2.909$ Å and $a = b = 2.911$ Å, respectively. All these results are consistent with previous reports [22, 43]. The bond lengths of monolayers are 1.95 Å for Ge-O, 2.09 Å for Mo-N, and 1.75 Å for Si-N. Figures 1(b) and (e) indicate that the GeO_2 and $MoSi_2N_4$ monolayers are semiconductors with indirect band structure, and the band gap of monolayer GeO_2 and $MoSi_2N_4$ is 3.56 (5.32) and 1.79 (2.35) eV for PBE (HSE06) calculation, respectively. In addition, Figs. 1(c) and (f) depict the phonon dispersion curves of GeO_2 and $MoSi_2N_4$ monolayers. Obviously, there are no imaginary

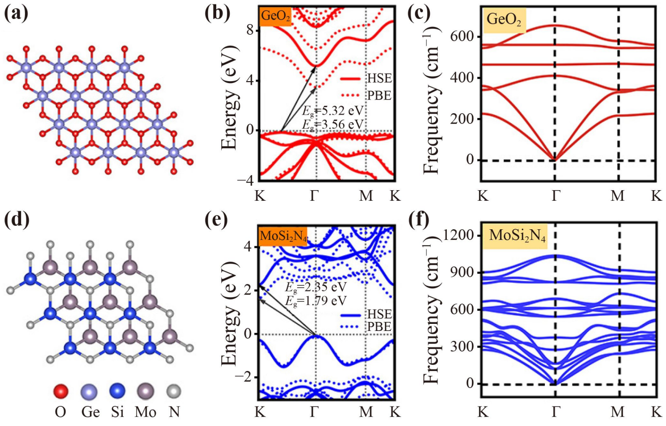

Fig. 1 **(a, d)** The atomic structures, **(b, e)** band structures, **(c, f)** phonon dispersion curves of GeO_2 and $MoSi_2N_4$ monolayers, respectively. The Fermi level is defined as zero. In the diagram of the atomic structures, different colored balls represent different atoms.

Table 1 The structural and electronic parameters. The lattice constant (a), interlayer distance (d), total energy (E_{total}), and band gap of PBE (E_g^{PBE}) and HSE06 (E_g^{HSE06}).

	a (Å)	d (Å)	E_{total} (eV)	E_g^{PBE} (eV)	E_g^{HSE06} (eV)
$MoSi_2N_4$	2.911	–	–61.603	1.79	2.35
GeO_2	2.909	–	–18.88	3.56	5.32
$GeO_2/MoSi_2N_4$	2.909	2.78	–82.816	0.275	0.946

phonon modes, which confirms the dynamical stability of the two kinds of 2D materials.

In order to obtain the credible structures of 2D GeO_2/$MoSi_2N_4$ vdWHs, a global structure search method is implemented. The total energy as a function of the in-plane shift is presented in Fig. 2(a). We consider 144 stacking structures $A_{m,n}$ passing through a 12 × 12 displacement grids. The $A_{m,n}$ means the displacement of the GeO_2 layer relative to the $MoSi_2N_4$ layer is $\left(\frac{m}{12}\right)\boldsymbol{a}+\left(\frac{n}{12}\right)\boldsymbol{b}$, where $\boldsymbol{a}$ and $\boldsymbol{b}$ are the lattice vectors of the vdWHs. Among them, the $A_{3,6}$ stacking pattern is the most stable structure with the interlayer distance between GeO_2 and $MoSi_2N_4$ layer of 2.78 Å. Also, Fig. 2(b) shows the side view of the most stable vdWHs structure consisting of GeO_2 and $MoSi_2N_4$ layer, in which the lattice mismatch is 0.07%. From the bright red region in Fig. 2(a), we find that there are four metastable structures around the $A_{3,6}$ stacking pattern, which feature that the total energy is close to that of the most stable structure. The total energy of these four metastable structures is shown in Table S1. In addition, Fig. S1 presents the projected band structures of the metastable and most stable structures calculated by the PBE and HSE06 methods. Similar total energy and electronic properties are given for the considered five configurations, and thus only the most stable structure is discussed in the following section. The HSE06 method is adopted for all the next calculations. Figure 2(c) indicates that GeO_2 and $MoSi_2N_4$ can form a type-II heterojunction with direct band gap of 0.946 eV. To further determine the dynamical stability of the structure with the lowest energy, Fig. 2(d) shows the phonon dispersion curves of the vdWHs, and all the phonon frequencies are positive, illustrating that the most stable GeO_2/$MoSi_2N_4$ vdWHs is also dynamically stable.

To further explore the electronic characteristics of the most stable structure GeO_2/$MoSi_2N_4$ vdWHs, Fig. 3 draws the orbital-projected electronic band structures, partial charge densities, plane-averaged differential charge density and electrostatic potential. As illustrated in Figs. 3(a) and (b), the CBM is mostly contributed by the Ge_s and O_p orbitals of the GeO_2 layer, while the VBM mainly comes from the N_p and Mo_d orbitals in the $MoSi_2N_4$ layer. Besides, the band shapes of GeO_2 and $MoSi_2N_4$ are well preserved after forming the heterojunction due to the vdWHs interaction. The charge distribution of Fig. 3(c) shows the CBM is mainly contributed by Ge and O atoms, and the VBM comes from Mo and N atoms, which coincides with the above discussion.

The plane-averaged charge density difference is calculated to assess the charge redistribution in the

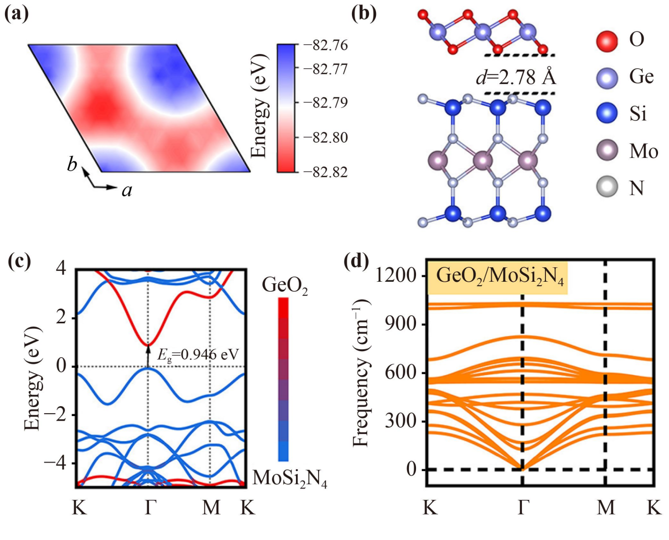

Fig. 2 **(a)** Color contour plot of total energy versus in-plane shift for GeO_2/$MoSi_2N_4$ vdWHs, considering the 12 × 12 grids. **(b)** The geometric structure, **(c)** band structure and **(d)** phonon dispersion curves of the most stable GeO_2/$MoSi_2N_4$ vdWHs. The Fermi level is defined as zero.

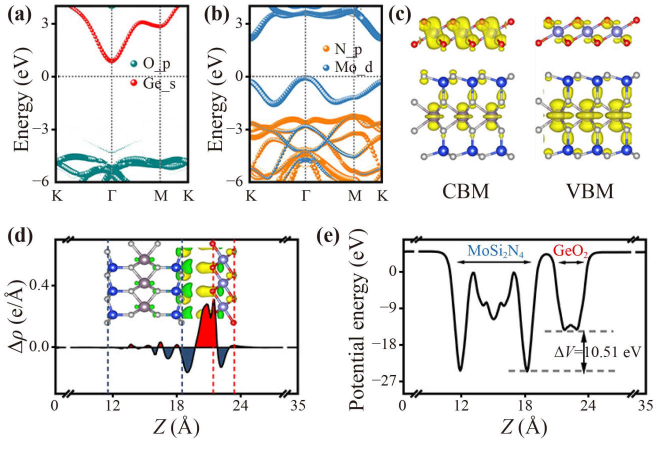

Fig. 3 The orbital-projected band structures of GeO_2/$MoSi_2N_4$ vdWHs on GeO_2 **(a)** and $MoSi_2N_4$ **(b)** layer. Partial charge density **(c)** and plane-averaged charge density difference **(d)** of GeO_2/$MoSi_2N_4$ vdWHs. Yellow (green) colored isosurfaces represent the charge accumulation (depletion), respectively. **(e)** Electrostatic potential of GeO_2/$MoSi_2N_4$ vdWHs. The isosurface is set to be 0.008 e/bohr^3 for (c) and 0.0001 e/ Å^3 for (d).

$GeO_2/MoSi_2N_4$ vdWHs, which can be calculated as $\Delta\rho = \rho_{vdWHs} - \rho_{GeO_2} - \rho_{MoSi_2N_4}$, where the ρ_{vdWHs}, ρ_{GeO_2}, and $\rho_{MoSi_2N_4}$ represent the charge density of the vdWHs, isolated GeO_2 and $MoSi_2N_4$ monolayers, respectively. In the inset of Fig. 3(d), the charge transfer mainly occurs at the interface of the vdWHs. The yellow and green region corresponds to the $\rho > 0$ and $\rho < 0$, indicating the accumulation and depletion of charge, respectively. Meanwhile, the charge is depleted near the $MoSi_2N_4$ layer and accumulated in the vicinity of the GeO_2 layer, which implies that the charge can be transferred from the $MoSi_2N_4$ layer to the GeO_2 layer.

In addition, the electrostatic potential along the perpendicular direction of the vdWHs is explored in Fig. 3(e). The potential drop (ΔV) across the two isolated layers is 10.51 eV, which indicates the presence of a strong built-in field across the interface. The electric field strength of $GeO_2/MoSi_2N_4$ vdWHs exceeds that of other $MoSi_2N_4$-based heterostructures, such as the $C_3N_4/MoSi_2N_4$ (6.28 eV) [38] and $MoSe_2/MoSi_2N_4$ (4.03 eV) [40]. The $MoSi_2N_4$ possesses a much deeper potential than GeO_2, owing to the stronger electronegativity of the $MoSi_2N_4$ monolayer. Thus, the deeper potential may facilitate the separation of electron-hole pairs, which is beneficial for photoelectric detection applications based on the $GeO_2/MoSi_2N_4$ vdWHs.

3.2 Biaxial strain tunable electronic properties of the vdWHs

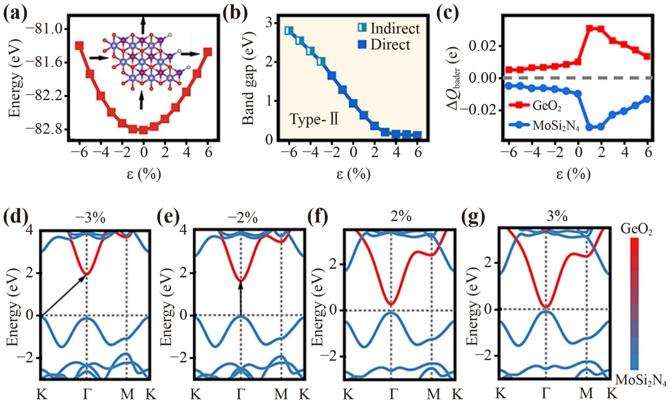

Fig. 4 The variation of the total energy **(a)**, band gap **(b)**, and interlayer charge transfer **(c)** of $GeO_2/MoSi_2N_4$ vdWHs as a function of biaxial strain, respectively. **(d–g)** Projected band structures of $GeO_2/MoSi_2N_4$ vdWHs with the biaxial strains of –3%, –2%, 2% and 3%.

Table 2 The bond lengths as a function of biaxial strain for $GeO_2/MoSi_2N_4$ vdWHs.

Strain	$d_{Ge\text{-}O}$ (Å)	$d_{Mo\text{-}N}$ (Å)	$d_{Si\text{-}N}$ (Å)
–6%	1.90	2.05	1.68
–5%	1.91	2.06	1.70
–4%	1.91	2.06	1.71
–3%	1.92	2.07	1.72
–2%	1.93	2.08	1.73
–1%	1.94	2.08	1.74
0	1.95	2.09	1.75
1%	1.96	2.10	1.76
2%	1.96	2.11	1.78
3%	1.97	2.12	1.79
4%	1.99	2.13	1.81
5%	2.00	2.14	1.82
6%	2.01	2.15	1.83

To understand the strain influence on the $GeO_2/MoSi_2N_4$ vdWHs, we define the biaxial strain as $\varepsilon = (a - a_0)/a_0$ on $GeO_2/MoSi_2N_4$ vdWHs, where a_0 and a represent the lattice parameter of heterostructures without and with biaxial strain, respectively. In Fig. 4, the negative and positive values are used to denote the compressive and tensile strain, respectively. Figures 4(a–c) display the variation of the total energy, band gap, and interlayer charge transfer of $GeO_2/MoSi_2N_4$ vdWHs under the biaxial strains. It is obvious from Fig. 4(a) that the total energy reaches the minimum value under the pristine condition. The band gap decreases for $GeO_2/MoSi_2N_4$ vdWHs with increasing tensile, which can be seen in Fig. 4(b). On the contrary, as the compressive strain is applied, the band gap value tends to increase. When the tensile strain increases up to 6%, the band gap of the vdWHs decreases from 0.946 eV to 0.124 eV. And the variation trend of the band gap gradually slows down and approaches saturation at 4% strain. Additionally, when the compressive strain range is 0 ~ –6%, the band gap increases linearly from 0.946 eV to 2.806 eV. Moreover, it can realize a transition from direct to indirect band gap when the compressive strain is greater than -3%. As shown in Table 2, we can see that with increasing the tensile strain for the $GeO_2/MoSi_2N_4$ vdWHs, the atomic bond lengths of Ge-O, Mo-N and Si-N can be raised, while the bond angles exhibit the reduced trend. In contrast to the case of tensile strain, the increasing compressive strain can make the Ge-O, Mo-N and Si-N bond lengths decrease, and the bond angles consequently enhance. However, it is worth noting that the type-II band arrangement is well preserved in the $GeO_2/MoSi_2N_4$ vdWHs under all the studied biaxial strain cases.

Figure 4(c) exhibits the evolution of interlayer charge transfer as a function of biaxial strain. The results show that the interlayer charge transfer of $GeO_2/MoSi_2N_4$ vdWHs decreases with increasing tensile and compressive strains. Under the case of tensile and compressive strain, the interlayer charge transfer declines by 0.018 e and 0.005 e, respectively. The charge transfer tends to diminish when the compressive strain is larger than –5%. Furthermore, it reaches a maximum value of 0.031 e under the 1% tensile strain.

To better understand the above-mentioned behavior, Figs. 4(d)–(g) present the projected band structures of

$GeO_2/MoSi_2N_4$ vdWHs under different biaxial strains. When tensile strain is applied, the conduction band edge moves to the Fermi level significantly, while the valence band edge barely moves, which is consistent with the decrease in the band gap. On the other side, the compressive strain causes the conduction band edge to move away from the Fermi level substantially, corresponding to the increase of the band gap. As the –2% compressive strain is applied, both CBM and VBM remain at Γ point. However, when the compressive strain is greater than –3%, the CBM of $GeO_2/MoSi_2N_4$ vdWHs is at Γ point, while the VBM is at K point, thus an indirect band gap can be observed. In particular, for all the studied strain cases, the CBM and VBM of $GeO_2/MoSi_2N_4$ vdWHs are always formed by the GeO_2 and $MoSi_2N_4$ layers, respectively, confirming that it always maintains type-II band alignment characteristics. In addition, we notice that the application of strain can induce the band alignment transition from type-II to type-I or type-III in many other 2D vdWHs, such as $GaSe/SnX_2$ (X = S, Se) [14], MoSSe/MBP [51] and BP/β-AsP vdWHs [52].

3.3 Interlayer distance tunable electronic properties of the vdWHs

The interlayer interaction has obvious effects on the electronic structures of the vdWHs. Thus, Fig. 5 plots the interlayer distance change on the electronic properties of the $GeO_2/MoSi_2N_4$ vdWHs. We can see from Fig. 5(a) that the curve of the total energy has the minimum energy value when the interlayer distance is 2.78 Å. From Fig. 5(b), the band gap increases for $GeO_2/MoSi_2N_4$ vdWHs with increasing interlayer distance. Also, the band gap changes slightly when the interlayer distance is larger than 3.28 Å. In addition, Fig. 5(c) shows that the interlayer charge transfer declines gradually with the increase of the interlayer distance. To reveal the related physical mechanism, in Figs. 5(d–g), we give the interlayer distance effects on the projected band structure of $GeO_2/MoSi_2N_4$ vdWHs. For different distances, the CBM and VBM contributions to $GeO_2/MoSi_2N_4$ vdWHs are provided by the GeO_2 and $MoSi_2N_4$ layers separately, showing that this type-II band alignment is insensitive to the interlayer interactions. Furthermore, the variation of the band gap is mainly due to the up and down movement of CBM.

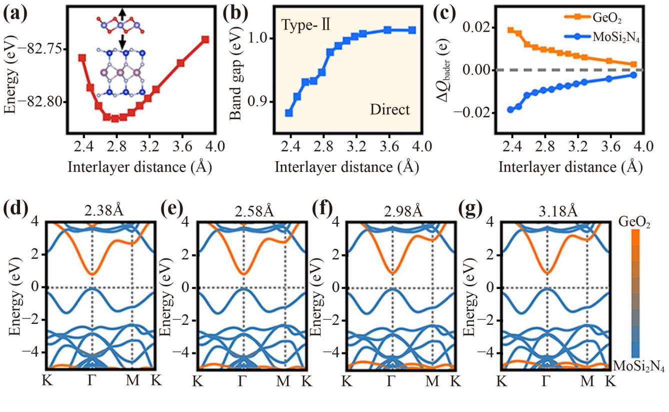

Fig. 5 The total energy **(a)** and band gap **(b)**, interlayer charge transfer **(c)** and projected band structures **(d–g)** of $GeO_2/MoSi_2N_4$ vdWHs at different interlayer distances, respectively.

3.4 Electric field tunable electronic properties of the vdWHs

The external vertical electric field provides another effective strategy for controlling the electronic structure. In the following, the variation of the band gap for $GeO_2/MoSi_2N_4$ vdWHs as a function of the electric field is shown in Fig. 6 (a). It should be noted that the electric field is perpendicular to the surface of the $GeO_2/MoSi_2N_4$ vdWHs, and the positive direction is defined from $MoSi_2N_4$ layer to GeO_2 layer, as illustrated in Fig. S2. When the electric field increases from –0.5 to 0.5 V/Å, the band gap decreases linearly, maintaining the type-II band alignment and direct band structures. Here, the band edge and projected band structures are also shown, and the reasons for the band alignment transition are discussed. In Fig. 6(b), with the increase of the external electric field, the CBM of $GeO_2/MoSi_2N_4$ vdWHs decreases significantly, while the VBM shifts upward slightly. Moreover, when the positive electric field reaches 0.4 V/Å, the VBM decreases more slightly, which causes the value of band gap to decrease slowly as the electric field changes from 0.4 V/Å to 0.5 V/Å. As can be seen from Figs. 6(c–f), with the increase of the positive electric field, the CBM of GeO_2 layer moves

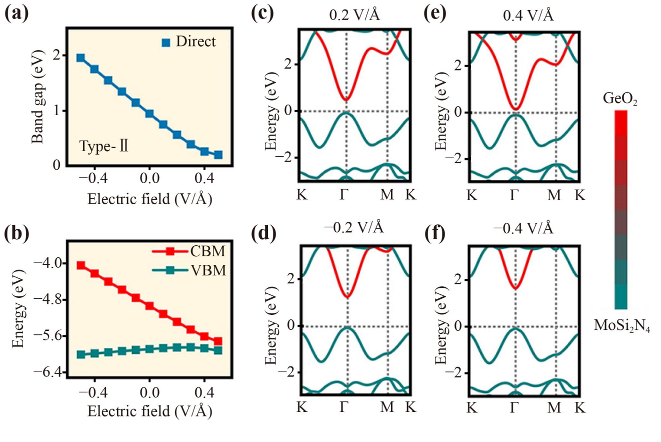

Fig. 6 The band gap **(a)** and band alignment **(b)** of $GeO_2/MoSi_2N_4$ vdWHs as a function of external electric field, respectively. **(c–f)** The projected band structures of $GeO_2/MoSi_2N_4$ vdWHs with different external electric fields. The red (green) line indicates the contribution of the GeO_2 ($MoSi_2N_4$) layer.

down gradually, while the CBM and VBM of $MoSi_2N_4$ keep almost unchanged. Compared with the 0.2 V/Å, the CBM of GeO_2 layer moves towards the Fermi level under the electric field of 0.4 V/Å. On the other hand, Fig. 6(f) indicates that with increasing the negative electric field, the CBM of GeO_2 layer moves away from the Fermi level when the electric field reaches –0.4 V/Å. However, further increased electric field does not change the type of band arrangement. Thus, the external electric field can change the band gap, while the band alignment remains type-II for the $GeO_2/MoSi_2N_4$ vdWHs. What's more, for many other vdWHs, the band alignment is sensitive to the external electric field [16, 51, 53–56]. For example, when the positive electric field is larger than 0.2 V/Å, the band alignment of the AlN/VSe_2 vdWHs changes from type-II to type-I [16]. The MoXY/WXY (X, Y = S, Se, Te; $X \neq Y$) vdWHs maintain robust type-II band alignment under positive electric field, while a reverse electric field can make the band alignment change [53].

4 Conclusions

In conclusion, by using a global structure search approach, we design the $GeO_2/MoSi_2N_4$ vdWHs to exactly explore the band structures, and the corresponding modulations of biaxial strain, electric field, and interlayer distance are considered to improve the performance of $GeO_2/MoSi_2N_4$ vdWHs. The results show that the monolayer GeO_2, $MoSi_2N_4$ and $GeO_2/MoSi_2N_4$ vdWHs are dynamically stable at room temperature. The most stable $GeO_2/MoSi_2N_4$ vdWHs possess direct band gap of 0.946 eV and type-II band alignment with the CBM and VBM from the GeO_2 and $MoSi_2N_4$ layers. When the biaxial strain is applied, the direct-to-indirect band gap transition can be achieved. More interestingly, the robust type-II band arrangement of $GeO_2/MoSi_2N_4$ vdWHs remains unchanged when the external electric field, interlayer distance, and biaxial strain are applied. These results reveal that the $GeO_2/MoSi_2N_4$ vdWHs can be in promising optoelectronic devices with stable characteristics due to their robust type-II band arrangement.

Electronic supplementary material Supplementary materials are available in the online version of this article at https://doi.org/10.1007/s11467-022-1216-8 and https://journal.hep.com.cn/fop/EN/10.1007/s11467-022-1216-8 and are accessible for authorized users.

Acknowledgements This work was supported by the National Natural Science Foundation of China under Grant Nos. 11904085 and 12074103. Program for Outstanding Youth of Henan Province under Grant No. 202300410221. Henan Normal University Innovative Science and Technology Team under Grant No. 20200185. The calculations were also supported by the High Performance Computing Center of Henan Normal University.

References

1. W. Wang, C. Si, W. Lei, F. Xiao, Y. Liu, C. Autieri, and X. Ming, Stacking order and Coulomb correlation effect in the layered charge density wave phase of 1T-NbS_2, *Phys. Rev. B* 105(3), 035119 (2022)
2. A. Aharon-Steinberg, A. Marguerite, D. J. Perello, K. Bagani, T. Holder, Y. Myasoedov, L. S. Levitov, A. K. Geim, and E. Zeldov, Long-range nontopological edge currents in charge-neutral graphene, *Nature* 593(7860), 528 (2021)
3. X. Li, P. Yuan, L. Li, M. He, J. Li, and C. Xia, Sub-5-nm monolayer GaSe MOSFET with ultralow subthreshold swing and high on-state current: Dielectric layer effect, *Phys. Rev. Appl.* 18(4), 044012 (2022)
4. T. Wang, A. Dong, X. Zhang, R. K. Hocking, and C. Sun, Theoretical study of K_3Sb/graphene heterostructure for electrochemical nitrogen reduction reaction, *Front. Phys.* 17(2), 23501 (2022)
5. Q. Q. Kong, X. G. An, J. Zhang, W. T. Yao, and C. H. Sun, Design of heterojunction with components in different dimensions for electrocatalysis applications, *Front. Phys.* 17(4), 43601 (2022)
6. C. Long, Y. Dai, Z. R. Gong, and H. Jin, Robust type-II band alignment in Janus-MoSSe bilayer with extremely long carrier lifetime induced by the intrinsic electric field, *Phys. Rev. B* 99(11), 115316 (2019)
7. N. Ubrig, E. Ponomarev, J. Zultak, D. Domaretskiy, V. Zolyomi, D. Terry, J. Howarth, I. Gutierrez-Lezama, A. Zhukov, Z. R. Kudrynskyi, Z. D. Kovalyuk, A. Patane, T. Taniguchi, K. Watanabe, R. V. Gorbachev, V. I. Fal'ko, and A. F. Morpurgo, Design of van der Waals interfaces for broad-spectrum optoelectronics, *Nat. Mater.* 19(3), 299 (2020)
8. J. G. Azadani, S. Lee, H. R. Kim, H. Alsalman, Y. K. Kwon, J. Tersoff, and T. Low, Simple linear response model for predicting energy band alignment of two-dimensional vertical heterostructures, *Phys. Rev. B* 103(20), 205129 (2021)
9. F. H. Davies, C. J. Price, N. T. Taylor, S. G. Davies, and S. P. Hepplestone, Band alignment of transition metal dichalcogenide heterostructures, *Phys. Rev. B* 103(4), 045417 (2021)
10. P. Rivera, J. R. Schaibley, A. M. Jones, J. S. Ross, S. Wu, G. Aivazian, P. Klement, K. Seyler, G. Clark, N. J. Ghimire, J. Yan, D. G. Mandrus, W. Yao, and X. Xu, Observation of long-lived interlayer excitons in monolayer $MoSe_2$–WSe_2 heterostructures, *Nat. Commun.* 6(1), 6242 (2015)
11. P. Rivera, K. L. Seyler, H. Yu, J. R. Schaibley, J. Yan, D. G. Mandrus, W. Yao, and X. Xu, Valley-polarized exciton dynamics in a 2D semiconductor heterostructure, *Science* 351(6274), 688 (2016)
12. Y. Y. Wang, F. P. Li, W. Wei, B. B. Huang, and Y. Dai, Interlayer coupling effect in van der Waals heterostructures of transition metal dichalcogenides, *Front. Phys.* 16(1), 13501 (2020)
13. X. Li, T. Liu, L. Li, M. He, C. Shen, J. Li, and C. Xia, Reconfigurable band alignment of m-GaS/n-XTe_2 (X = Mo, W) multilayer van der Waals heterostructures for

photoelectric applications, *Phys. Rev. B* 106(12), 125306 (2022)

14. D. Wijethunge, L. Zhang, C. Tang, and A. Du, Tuning band alignment and optical properties of 2D van der Waals heterostructure via ferroelectric polarization switching, *Front. Phys.* 15(6), 63504 (2020)
15. S. Ghosh, A. Varghese, H. Jawa, Y. Yin, N. V. Medhekar, and S. Lodha, Polarity-tunable photocurrent through band alignment engineering in a high-speed $WSe_2/SnSe_2$ diode with large negative responsivity, *ACS Nano* 16(3), 4578 (2022)
16. Y. Zhu, D. Zhang, H. Ye, D. Bai, M. Li, G. P. Zhang, J. Zhang, and J. Wang, Magnetic and electronic properties of AlN/VSe_2 van der Waals heterostructures from combined first-principles and Schrödinger–Poisson simulations, *Phys. Rev. Appl.* 18(2), 024012 (2022)
17. Y. L. Hong, Z. Liu, L. Wang, T. Zhou, W. Ma, C. Xu, S. Feng, L. Chen, M. L. Chen, D. M. Sun, X. Q. Chen, H. M. Cheng, and W. Ren, Chemical vapor deposition of layered two-dimensional $MoSi_2N_4$ materials, *Science* 369(6504), 670 (2020)
18. R. Islam, B. Ghosh, C. Autieri, S. Chowdhury, A. Bansil, A. Agarwal, and B. Singh, Tunable spin polarization and electronic structure of bottom-up synthesized $MoSi_2N_4$ materials, *Phys. Rev. B* 104(20), L201112 (2021)
19. A. Bafekry, M. Faraji, M. M. Fadlallah, A. Bagheri Khatibani, A. abdolahzadeh Ziabari, M. Ghergherehchi, S. Nedaei, S. F. Shayesteh, and D. Gogova, Tunable electronic and magnetic properties of $MoSi_2N_4$ monolayer via vacancy defects, atomic adsorption and atomic doping, *Appl. Surf. Sci.* 559, 149862 (2021)
20. Q. Wu, L. Cao, Y. S. Ang, and L. K. Ang, Semiconductor-to-metal transition in bilayer $MoSi_2N_4$ and WSi_2N_4 with strain and electric field, *Appl. Phys. Lett.* 118(11), 113102 (2021)
21. H. Zhong, W. Xiong, P. Lv, J. Yu, and S. Yuan, Strain-induced semiconductor to metal transition in MA_2Z_4 bilayers (M=Ti, Cr, Mo; A=Si; Z=N, P), *Phys. Rev. B* 103(8), 085124 (2021)
22. S. Li, W. Wu, X. Feng, S. Guan, W. Feng, Y. Yao, and S. A. Yang, Valley-dependent properties of monolayer $MoSi_2N_4$, WSi_2N_4, and $MoSi_2As_4$, *Phys. Rev. B* 102(23), 235435 (2020)
23. T. Zhong, Y. Ren, Z. Zhang, J. Gao, and M. Wu, Sliding ferroelectricity in two-dimensional MoA_2N_4 (A = Si or Ge) bilayers: High polarizations and Moiré potentials, *J. Mater. Chem. A* 9(35), 19659 (2021)
24. L. Wang, Y. Shi, M. Liu, A. Zhang, Y. L. Hong, R. Li, Q. Gao, M. Chen, W. Ren, H. M. Cheng, Y. Li, and X. Q. Chen, Intercalated architecture of MA_2Z_4 family layered van der Waals materials with emerging topological, magnetic and superconducting properties, *Nat. Commun.* 12(1), 2361 (2021)
25. Q. Wu and L. K. Ang, Giant tunneling magnetoresistance in atomically thin $VSi_2N_4/MoSi_2N_4/VSi_2N_4$ magnetic tunnel junction, *Appl. Phys. Lett.* 120(2), 022401 (2022)
26. Y. Zang, Q. Wu, W. Du, Y. Dai, B. Huang, and Y. Ma, Activating electrocatalytic hydrogen evolution performance of two-dimensional MSi_2N_4(M=Mo, W): A theoretical prediction, *Phys. Rev. Mater.* 5(4), 045801 (2021)
27. J. Yuan, Q. Wei, M. Sun, X. Yan, Y. Cai, L. Shen, and U. Schwingenschlögl, Protected valley states and generation of valley- and spin-polarized current in monolayer MA_2Z_4, *Phys. Rev. B* 105(19), 195151 (2022)
28. B. Mortazavi, B. Javvaji, F. Shojaei, T. Rabczuk, A. V. Shapeev, and X. Y. Zhuang, Exceptional piezoelectricity, high thermal conductivity and stiffness and promising photocatalysis in two-dimensional $MoSi_2N_4$ family confirmed by first-principles, *Nano Energy* 82, 105716 (2021)
29. Y. Yin, M. Yi, and W. Guo, High and anomalous thermal conductivity in monolayer MSi_2Z_4 semiconductors, *ACS Appl. Mater. Interfaces* 13(38), 45907 (2021)
30. C. C. Jian, X. C. Ma, J. Q. Zhang, and X. Yong, Strained $MoSi_2N_4$ monolayers with excellent solar energy absorption and carrier transport properties, *J. Phys. Chem. C* 125(28), 15185 (2021)
31. A. Bafekry, C. Stampfl, M. Naseri, M. M. Fadlallah, M. Faraji, M. Ghergherehchi, D. Gogova, and S. A. H. Feghhi, Effect of electric field and vertical strain on the electro–optical properties of the $MoSi_2N_4$ bilayer: A first-principles calculation, *J. Appl. Phys.* 129(15), 155103 (2021)
32. L. Cao, G. Zhou, Q. Wang, L. K. Ang, and Y. S. Ang, Two-dimensional van der Waals electrical contact to monolayer $MoSi_2N_4$, *Appl. Phys. Lett.* 118(1), 013106 (2021)
33. J. Zhao, X. H. Jin, H. Zeng, C. Yao, and G. Yan, Spin-valley coupling and valley splitting in the $MoSi_2N_4/CrCl_3$ van der Waals heterostructure, *Appl. Phys. Lett.* 119(21), 213101 (2021)
34. Y. Ding and Y. Wang, First-principles study of two-dimensional $MoN_2X_2Y_2$ (X = B~In, Y = N~Te) nanosheets: The III–VI analogues of $MoSi_2N_4$ with peculiar electronic and magnetic properties, *Appl. Surf. Sci.* 593, 153317 (2022)
35. C. Nguyen, N. V. Hoang, H. V. Phuc, A. Y. Sin, and C. V. Nguyen, Two-dimensional boron phosphide/$MoGe_2N_4$ van der Waals heterostructure: A promising tunable optoelectronic material, *J. Phys. Chem. Lett.* 12(21), 5076 (2021)
36. Y. Guo, Y. Dong, X. Cai, L. Liu, and Y. Jia, Controllable Schottky barriers and contact types of BN intercalation layers in graphene/$MoSi_2As_4$ vdW heterostructures via applying an external electrical field, *Phys. Chem. Chem. Phys.* 24(30), 18331 (2022)
37. Z. Zhang, G. Chen, A. Song, X. Cai, W. Yu, X. Jia, and Y. Jia, Optoelectronic properties of bilayer van der Waals $WSe_2/MoSi_2N_4$ heterostructure: A first-principles study, *Physica E* 144, 115429 (2022)
38. C. Q. Nguyen, Y. S. Ang, S. T. Nguyen, N. V. Hoang, N. M. Hung, and C. V. Nguyen, Tunable type-II band alignment and electronic structure of $C_3N_4/MoSi_2N_4$ heterostructure: Interlayer coupling and electric field, *Phys. Rev. B* 105(4), 045303 (2022)
39. Y. T. Ren, L. Hu, Y. T. Chen, Y. J. Hu, J. L. Wang, P. L. Gong, H. Zhang, L. Huang, and X. Q. Shi, Two-dimensional MSi_2N_4 monolayers and van der Waals heterostructures: Promising spintronic properties and band alignments, *Phys. Rev. Mater.* 6(6), 064006 (2022)

40. X.Cai, Z. Zhang, Y. Zhu, L. Lin, W. Yu, Q. Wang, X. Yang, X. Jia, and Y. Jia, A two-dimensional $MoSe_2$/$MoSi_2N_4$ van der Waals heterostructure with high carrier mobility and diversified regulation of its electronic properties, *J. Mater. Chem. C* 9(31), 10073 (2021)
41. A. Bafekry, M. Faraji, A. Abdollahzadeh Ziabari, M. M. Fadlallah, C. V. Nguyen, M. Ghergherehchi, and S. A. H. Feghhi, A van der Waals heterostructure of MoS_2/$MoSi_2N_4$: a first-principles study, *New J. Chem.* 45(18), 8291 (2021)
42. J. Q. Ng, Q. Wu, L. K. Ang, and Y. S. Ang, Tunable electronic properties and band alignments of $MoSi_2N_4$/GaN and $MoSi_2N_4$/ZnO van der Waals heterostructures, *Appl. Phys. Lett.* 120(10), 103101 (2022)
43. Y. Sozen, M. Yagmurcukardes, and H. Sahin, Vibrational and optical identification of GeO_2 and GeO single layers: A first-principles study, *Phys. Chem. Chem. Phys.* 23(37), 21307 (2021)
44. S. Chuang, C. Battaglia, A. Azcatl, S. McDonnell, J. S. Kang, X. Yin, M. Tosun, R. Kapadia, H. Fang, R. M. Wallace, and A. Javey, MoS_2 p-type transistors and diodes enabled by high work function MoO_x contacts, *Nano Lett.* 14(3), 1337 (2014)
45. H. Kim and H. J. Choi, Thickness dependence of work function, ionization energy, and electron affinity of Mo and W dichalcogenides from DFT and GW calculations, *Phys. Rev. B* 103(8), 085404 (2021)
46. B. Y. Zhang, K. Xu, Q. Yao, A. Jannat, G. Ren, M. R. Field, X. Wen, C. Zhou, A. Zavabeti, and J. Z. Ou, Hexagonal metal oxide monolayers derived from the metal-gas interface, *Nat. Mater.* 20(8), 1073 (2021)
47. G. Kresse and J. Furthmuller, Efficient iterative schemes for *ab initio* total-energy calculations using a plane-wave basis set, *Phys. Rev. B* 54(16), 11169 (1996)
48. J. P. Perdew, K. Burke, and M. Ernzerhof, Generalized gradient approximation made simple, *Phys. Rev. Lett.* 77(18), 3865 (1996)
49. J. Heyd, G. E. Scuseria, and M. Ernzerhof, Hybrid functionals based on a screened Coulomb potential, *J. Chem. Phys.* 118(18), 8207 (2003)
50. G. Kresse and D. Joubert, From ultrasoft pseudopotentials to the projector augmented-wave method, *Phys. Rev. B* 59(3), 1758 (1999)
51. Y. Mogulkoc, R. Caglayan, and Y. O. Ciftci, Band alignment in monolayer boron phosphide with Janus MoSSe heterobilayers under strain and electric field, *Phys. Rev. Appl.* 16(2), 024001 (2021)
52. Y. L. Liu, Y. Shi, H. Yin, and C. L. Yang, Two-dimensional BP/β-AsP van der Waals heterostructures as promising photocatalyst for water splitting, *Appl. Phys. Lett.* 117(6), 063901 (2020)
53. S. Patel, U. Dey, N. P. Adhikari, and A. Taraphder, Electric field and strain-induced band-gap engineering and manipulation of the Rashba spin splitting in Janus van der Waals heterostructures, *Phys. Rev. B* 106(3), 035125 (2022)
54. M. Yagmurcukardes, E. Torun, R. T. Senger, F. M. Peeters, and H. Sahin, $Mg(OH)_2$–WS_2 van der Waals heterobilayer: Electric field tunable band-gap crossover, *Phys. Rev. B* 94(19), 195403 (2016)
55. K. Iordanidou and J. Wiktor, Two-dimensional $MoTe_2$/$SnSe_2$ van der Waals heterostructures for tunnel-FET applications, *Phys. Rev. Mater.* 6(8), 084001 (2022)
56. K. Liang, T. Huang, K. Yang, Y. Si, H. Y. Wu, J. C. Lian, W. Q. Huang, W. Y. Hu, and G. F. Huang, Dipole engineering of two-dimensional van der Waals heterostructures for enhanced power-conversion efficiency: The case of Janus Ga_2SeTe/InS, *Phys. Rev. Appl.* 16(5), 054043 (2021)